Flow Measurement and Instrumentation 51 (2016) 8–20

Contents lists available at ScienceDirect

Flow Measurement and Instrumentation

journal homepage: www.elsevier.com/locate/flowmeasinst

Total pressure fluctuations and two-phase flow turbulence in self-aerated stepped chute flows

Gangfu Zhang, Hubert Chanson*, Hang Wang

The University of Queensland, School of Civil Engineering, Brisbane QLD 4072, Australia

ARTICLE INFO

Article history:
Received 9 January 2016
Received in revised form
8 August 2016
Accepted 12 August 2016
Available online 13 August 2016

Keywords:
Total pressure fluctuations
Two-phase flow
Turbulence
Self-aeration
Stepped spillways

ABSTRACT

Current knowledge in high-velocity self-aerated flows continues to rely upon physical modelling. Herein a miniature total pressure probe was successfully used in both clear-water and air-water flow regions of high-velocity open channel flows on a steep stepped channel. The measurements were conducted in a large size facility (θ=45°, h=0.1 m, W=0.985 m) and they were complemented by detailed clear-water and air-water flow measurements using a Prandtl-Pitot tube and dual-tip phase-detection probe respectively in both developing and fully-developed flow regions for Reynolds numbers within 3.3×10^5 to 8.7×10^5. Upstream of the inception point of free-surface aeration, the clear-water developing flow was characterised by a developing turbulent boundary layer and an ideal-flow region above. The boundary layer flow presented large total pressure fluctuations and turbulence intensities, with distributions of turbulence intensity close to intermediate roughness flow data sets: i.e., intermediate between d-type and k-type. The total pressure measurements were validated in the highly-aerated turbulent shear region, since the total pressure predictions based upon simultaneously-measured void fraction and velocity data agreed well with experimental results recorded by the total pressure probe. The results demonstrated the suitability of miniature total pressure probe in both monophase and two-phase flows. Both interfacial and water phase turbulence intensities were recorded. Present findings indicated that the turbulence intensity in the water phase was smaller than the interfacial turbulence intensity.

1. Introduction

Dams and reservoirs are man-made hydraulic structures built across rivers and streams to provide water storage. During major rainfalls, the large inflows into a reservoir induce a rise in water level associated with the risk of dam overtopping, unless a spillway system is designed. Most dams are equipped with an overflow system, consisting of a crest, a steep chute and a downstream energy dissipator [31,37,46]. On the steep chute, the flow is accelerated by gravity and a turbulent boundary layer develops at the upstream end. When the outer edge of the boundary layer interacts with the free-surface, the turbulent shear stresses next to the air-water interface may overcome both the surface tension and buoyancy effects, and free-surface aeration takes place [14,24]. This location is called the inception point of free-surface aeration [34,49]. Fig. 1 illustrates the overflow down a steep chute, and the inception point of free-surface aeration is clearly seen in Figs. 1A and B. Downstream self-aeration is commonly observed and the process is called 'white waters' [7,23,43,48] (Fig. 1). The physical processes are basically identical for smooth-invert and stepped spillways, although the latters are characterised by a greater rate of energy dissipation [11].

Current knowledge in high-velocity self-aerated flows relies heavily upon physical modelling and measurements, because of the large number of relevant equations and parameters [5,22,30]. Traditional monophase flow metrology may be used in the developing flow region, although velocity measurements are difficult close to the free-surface [1,36,38]. Accurate measurements in the air-water flow region rely upon intrusive phase-detection probes and hot-film probes. Review papers include Cain and Wood [8], Chanson [13], Chang et al. [10] and Chanson and Carosi [15].

In the present study, it is shown that a miniature total pressure probe may provide detailed informations in both clear-water and air-water flow regions. The metrology was applied to high-velocity open channel flows on a steep stepped channel. The measurements were conducted in a large size facility (θ=45°, h=0.1 m, W=0.985 m) in which detailed turbulent flow properties were recorded systematically in both developing and fully-developed flow regions for several discharges, corresponding to Reynolds numbers within 3.3×10^5 to 8.7×10^5.

* Corresponding author.
E-mail address: h.chanson@uq.edu.au (H. Chanson).

http://dx.doi.org/10.1016/j.flowmeasinst.2016.08.007

Nomenclature

C	time-averaged void fraction defined as the volume of air per unit volume of air and water;
D_H	hydraulic diameter (m) also called equivalent pipe diameter;
d	clear water flow depth (m) measured normal to the pseudo-bottom formed by the step edges;
d_c	critical flow depth (m) : $d_c = \sqrt[3]{Q^2/(g\ W^2)}$;
F	bubble count rate (Hz) or bubble frequency defined as the number of detected air bubbles per unit time;
g	gravity constant: g=9.80 m/s^2 in Brisbane, Australia;
H_1	upstream head above crest (m);
h	vertical step height (m);
L_{xx}	air-water advection integral length scale (m): $L_{xx}=V_x T_{xx}$;
$(L_{xx})_{max}$	maximum advection air-water length scale (m) in a cross-section;
k_s	step cavity roughness height (m): $k_s = h \times \cos\theta$;
k_s'	equivalent sand roughness height (m);
L_{crest}	crest length (m);
l	horizontal step length (m);
N	power law exponent;
P_k	kinetic pressure (Pa);
P_s	static pressure (Pa);
P_t	total pressure (Pa): $P_t=P_k+P_s$;
p_k	kinetic pressure fluctuation (Pa);
p_s	static pressure fluctuation (Pa);
p_t	total pressure fluctuation (Pa);
$\overline{p_k^2}$	variance of kinetic pressure (Pa^2);
$\overline{p_s^2}$	variance of static pressure (Pa^2);
$\overline{p_t^2}$	variance of total pressure (Pa^2);
Q	water discharge (m^3/s);
Re	Reynolds number defined in terms of the hydraulic diameter;
R_{xx}	normalised auto-correlation function;
r_{pu}	correlation between static pressure and streamwise velocity fluctuations: $r_{pu} = \overline{p_s\, v_x}/\left(\sqrt{\overline{v_x^2}}\sqrt{\overline{p_s^2}}\right)$
Tu	interfacial turbulence intensity: $Tu = \sqrt{\overline{v_{aw}^2}}/V_{aw}$;
Tu_p	turbulence intensity in the water phase defined as: $Tu_p = \sqrt{\overline{v_x^2}}/V_x$;
T_X	integral turbulent time scale (s) characterising large eddies advecting the air bubbles;
T_{xx}	auto-correlation time scale (s): $T_{xx} = \int_0^{t_{Rxx=0}} R_{xx}(t)\,dt$
t	time lag (s);
V_{aw}	interfacial velocity (m/s);
V_c	critical flow velocity (m/s);
V_x	streamwise velocity component in water phase (m/s);
V_{90}	characteristic interfacial velocity (m/s) where C=0.90;
v_{aw}	fluctuation of interfacial velocity (m/s);
v_x	fluctuation of streamwise velocity component in water phase (m/s);
$\overline{v_{aw}^2}$	variance of longitudinal component of interfacial velocity (m^2/s^2);
$\overline{v_x^2}$	variance of longitudinal component of water phase velocity (m^2/s^2);
W	channel width (m);
x	distance along the channel bottom (m);
Y_{90}	characteristic depth (m) where the void fraction is 90%;
y	distance (m) measured normal to the invert (or channel bed);
z	transverse distance (m) from the channel centreline;

Greek symbols

δ	boundary layer thickness (m);
μ_w	water dynamic viscosity (Pa s);
θ	angle between the pseudo-bottom formed by the step edges and the horizontal;
ρ	density (kg/m^3);
ρ_w	water density (kg/m^3);
σ	surface tension between air and water (N/m);
τ	time lag (s);
∅	diameter (m);

Subscript

aw	interfacial flow data;
p	total pressure data;
w	water properties;
xx	auto-correlation;
50	flow conditions where C=0.50;
90	flow conditions where C=0.90.

2. Physical modelling, experimental facility and instrumentation

2.1. Presentation

Steep chute flows are characterised by intense turbulence and interfacial interactions. Physical modelling is typically performed in a down-sized version of the prototype (Fig. 1). A full dynamic similarity is necessary for the laboratory model (Fig. 1B) to accurately predict a range of prototype characteristics (Fig. 1A). On a stepped chute, a simplistic dimensional analysis implies that the flow properties in the developing flow region must satisfy:

$$\frac{d}{d_c}, \frac{V_x}{V_c}, \frac{v_x}{V_c}, \frac{P_t}{\rho_w g\ d_c}, \frac{P_s}{\rho_w g\ d_c}, \frac{p_t}{\rho_w g\ d_c}\frac{p_s}{\rho_w g\ d_c}, \ldots = F_1\left(\frac{x}{d_c}, \frac{y}{d_c}, \frac{z}{d_c}, \frac{d_c}{h}, \frac{\rho_w V_x D_H}{\mu_w}, \frac{g\,\mu_w^4}{\rho\ \sigma^3}, \frac{W}{d_c}, \theta, \frac{k_s'}{d_c}, \ldots\right) \quad (1)$$

where d is the water depth, V_x is the mean streamwise water velocity, v_x is the streamwise water turbulent velocity fluctuation, P_t and p_t are the mean and fluctuating total pressure, P_s and p_s are the mean and fluctuating static pressure, g is the gravity constant, d_c is the critical depth: $d_c=(Q^2/(g\ W))^{1/3}$ with Q the water discharge and W the chute width, V_c is the critical velocity: $V_c=(g\ d_c)^{1/2}$, ρ_w is the water density, x, y and z are respectively the streamwise, normal and transverse coordinates, h is the step height, D_H is the hydraulic diameter, μ_w is the dynamic viscosity of water, σ is the surface tension of water, θ is the chute slope, and k_s' is the equivalent sand roughness of the step surface (Fig. 1C). In the fully-developed air-water flow region, dimensional analysis yields a different expression:

$$C, \frac{V_{aw}}{V_c}, \frac{v_{aw}}{V_c}, \frac{F\ d_c}{V_c}, \frac{P_t}{\rho_w g\ d_c}, \frac{P_s}{\rho_w g\ d_c}, \frac{p_t}{\rho_w g\ d_c}\frac{p_s}{\rho_w g\ d_c}, \ldots = F_2\left(\frac{x}{d_c}, \frac{y}{d_c}, \frac{z}{d_c}, \frac{d_c}{h}, \frac{\rho_w V_{aw} D_H}{\mu_w}, \frac{g\,\mu_w^4}{\rho\ \sigma^3}, \frac{W}{d_c}, \theta, \frac{k_s'}{d_c}, \ldots\right) \quad (2)$$

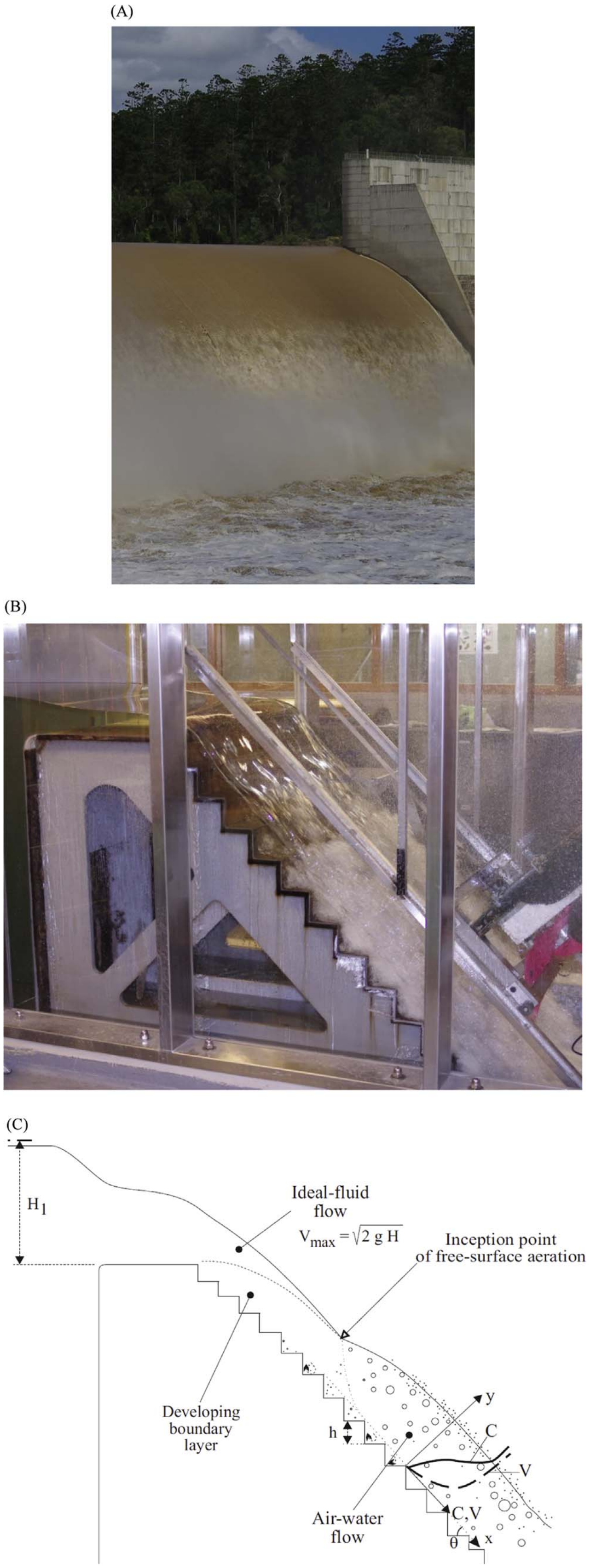

Fig. 1. High-velocity self-aerated flows down stepped chutes. (A) Paradise Dam stepped spillway in operation on 5 March 2013 (θ=57.4°, h=0.62 m, Q=2,320 m^3/s, d_c/h=2.85, Re=2.9 × 10^7), (B) Physical model in operation (θ=45°, h=0.10 m, Q=0.085 m^3/s, d_c/h=0.9, Re=3.6 × 10^5), (C) Definition sketch.

where C is the void fraction, V_{aw} is the interfacial velocity, v_{aw} is the streamwise interfacial velocity fluctuation, and F is the bubble count rate.

In Eqs. (1) and (2), the developing clear-water and fully-developed air-water flow properties at a given location (x, y, z) are expressed as functions of the Froude, Reynolds and Morton numbers (4th, 5th and 6th terms) and channel properties. Note that the dimensionless discharge d_c/h is equivalent to a Froude number defined in terms of the step height Herein a Froude similitude was adopted based upon Eqs. (1) and (2). The dependence on the Reynolds number implied potential scale effects since the Reynolds numbers in laboratory were smaller than in prototypes. The facility was operated at relatively high Reynolds numbers up to 8.7 × 10^5 to minimise potential scale effects. Lastly the fluid properties were invariant; thus the Morton number was an invariant.

2.2. Experimental facility and instrumentation

Physical experiments were conducted in a large stepped spillway model (1 V:1 H) located at the University of Queensland (Fig. 1B). The test section had a footprint of 4.6 × 0.985 m^2. It consisted of a 0.6 m long and 0.985 m wide broad crest with a 1.2 m high vertical upstream wall, an upstream rounded nose (0.058 m radius), and a downstream rounded edge (0.012 m radius) The weir was followed by a steep chute consisting of 12 steps: each step was 0.1 m long, 0.1 m high and 0.985 m wide. A smooth and stable discharge was delivered by three pumps driven by adjustable frequency AC motors. Water was fed into a 1.7 m deep, 5 m wide intake basin with a footprint of 2.7 × 5 m^2, leading to a 2.8 m long side-wall convergent with a contraction ratio of 5.08:1, resulting in a smooth and waveless inflow into the test section. The water discharge was deduced from detailed velocity and pressure measurements above the broad crested weir [50]:

$$\frac{Q}{W} = \left(0.8966 + 0.243\frac{H_1}{L_{crest}}\right)\sqrt{g\left(\frac{2}{3}H_1\right)^3} \tag{3}$$

where W is the crest width (W=0.985 m), H_1 is the total upstream head above crest, and L_{crest} is the crest length (L_{crest}=0.60 m) (Fig. 1C).

Clear-water flow depths were measured with a pointer-gauge on the channel centreline, as well as using photographic observations and performing cheques with a phase detection probe. Velocity measurements were performed in the clear water developing flow region with a Dwyer® 166 Series Prandtl-Pitot tube (Ø=3.18 mm). The tube was equipped with a hemispherical total pressure tapping and four equally spaced static pressure tappings located 25.4 mm behind the tip. The longitudinal separation between the total and static tappings was taken into account, by repeating independently measurements at each location.

The instantaneous total pressures were recorded with a micro-electro-mechanical-system (MEMS) MeasureX MRV21 miniature pressure transducer with an inner diameter of 1 mm and an outer diameter of 5 mm. The sensor featured a silicon diaphragm, with minimal static and thermal errors. The transducer was custom-designed to measure relative pressures ranging between 0 and 0.15 bars with a precision of 0.5% full scale (FS). Note that the sensor could not measure sub-atmospheric pressures with any degree of reliability. The signal was amplified and low-pass filtered at a cut off frequency of 2 kHz. A sampling frequency of 5 kHz was selected to minimise information loss [47]. The sampling duration was 60 s in the clear-water developing flow region and 180 s in the air-water fully-developed flow region during simultaneous sampling with the phase-detection probe.

(A)

(B)

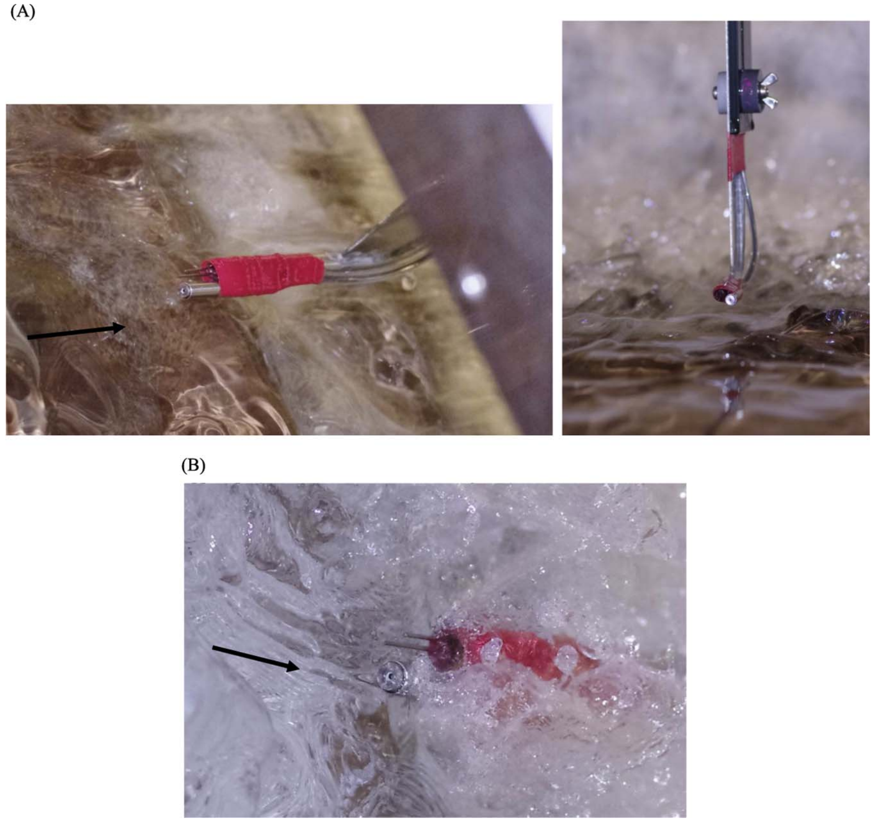

Fig. 2. Phase-detection and total pressure probes mounted side-by-side with 6.5 mm between total pressure sensor centreline and leading tip of phase-detection probe - Flow conditions: $d_c/h = 1.3$, $Re = 5.8 \times 10^5$, arrow points to the flow direction. (A) Probes located above the clear-water flow region, (B) Probes located in the upper spray above the air-water flow region (view in elevation).

Air-water flow measurements were conducted using dual-tip phase detection probes developed and built at the University of Queensland [13]. The probe consisted of two tips, each having an inner diameter of 0.25 mm and an outer diameter of 0.8 mm. The inner and outer electrodes of each tip were respectively made of silver and stainless steel. The longitudinal separation between the tips for each probe was between 6.9 mm and 8.0 mm depending upon the probe. The probe was excited by an electronic system (Ref. UQ82.518) designed with a response time less than 10 µs. Each probe tip signal was recorded at a sampling rate of 20 kHz for a duration of 45 s, selected based upon previous sensitivity analyses [26,45]. The sampling rate and duration were 5 kHz and 180 s respectively during simultaneous sampling with the pressure sensor (Fig. 2). In that case, the total pressure probe tip was at the same elevation as and 6 mm aside the leading tip of the double-tip phase-detection probe.

A trolley system was used to support and position the probes (Pitot, total pressure, phase-detection). The longitudinal movement was fixed by steel rails parallel to the pseudo-bottom formed by the step edges and the normal movement was controlled by a Mitutoyo™ digital ruler to achieve an accuracy of ± 0.01 mm.

2.3. Total pressure signal analysis

The total pressure sensor measured the instantaneous total pressure in the direction aligned with the sensor:

$$\tilde{P}_t = \frac{1}{2}\tilde{\rho}\,\tilde{V}_x^2 + \tilde{P}_s \tag{4}$$

where $\tilde{P}_t$ is the instantaneous total pressure, $\tilde{\rho}$ is the instantaneous fluid density, $\tilde{V}_x$ is the instantaneous streamwise fluid velocity detected by the sensor, and $\tilde{P}_s$ is the instantaneous static pressure. In the followings capital and lower case letters are used to denote mean and fluctuating quantities; for example, $\tilde{P}_t = P_t + p_t$.

In clear water flows, the relationship between turbulence intensity and root mean square of total pressure fluctuation may be derived:

$$Tu_p = \sqrt{\frac{\overline{p_t^2}}{\rho_w^2\ V_x^4}} \tag{5}$$

where $Tu_p = \sqrt{\overline{v_x^2}}/V_x$ and V_x is the streamwise velocity component in the water. Eq. (5) is similar to an expression derived by Arndt and Ippen [3] (see discussion in Appendix I).

In a two-phase flow, the total pressure output showed a distinct bimodal distribution because of the effects of air bubbles. This is illustrated by the probability density functions (PDF) of the total pressure probe signals (Fig. 3). In Fig. 3, the first signal probability distribution function (PDF) shows a unimodal distribution because of the small number of air bubbles ($C = 0.008$, purple line), where C is the time-averaged void fraction and F the bubble count rate. The other two PDFs exhibit large peaks next to zero, likely linked to interfacial and capillary effects during air bubble impacts on the total pressure sensor. Neglecting the air density and capillary effects and for $Tu_p \leq 0.4$–0.5, the relationship between total pressure fluctuation and turbulence intensity yields:

$$Tu_p = \sqrt{\frac{\frac{\overline{p_t^2}}{\rho_w^2\ V_x^4} - \frac{(1-C)\,C}{4}}{(1-C)\left(1+\frac{C}{2}\right)}} \tag{6}$$

where Tu_p is the water-phase turbulence intensity, C is the time-averaged void fraction and V_x was assumed to be equal to the interfacial velocity: $V_x \approx V_{aw}$. More generally, the higher order

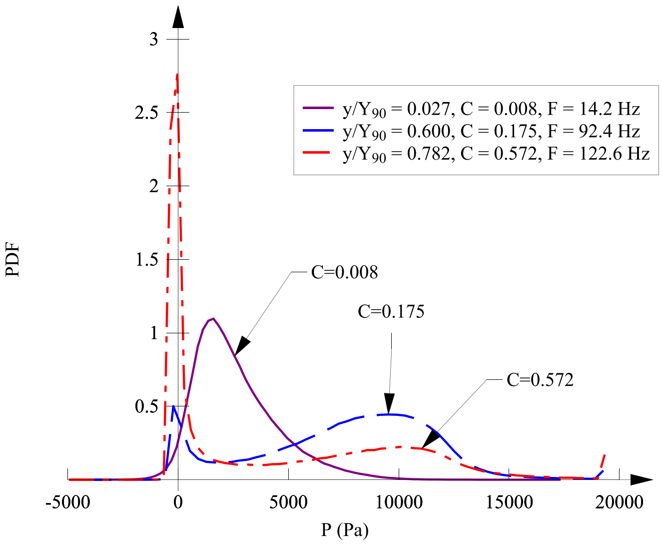

Fig. 3. Bimodal distributions of total pressure probe output – Flow conditions: $\theta=45°$, $h=0.1$ m, $d_c/h=1.7$, $Re=8.7\times10^5$, step edge 12.

terms (i.e. Tu_p^3, Tu_p^4) may not be neglected, and a more complete relationship between total pressure fluctuation and turbulence intensity is (Appendix I):

$$\frac{\overline{p_t^2}}{\rho_w^2\ V_x^4} = \left((1-C)\left(\frac{1}{2}+\frac{C}{4}\right)+0.34(1-C)^2\right)Tu_p^4 - 0.116(1-C)^2 Tu_p^3 + (1-C)\left(1+\frac{1}{2}C\right)\ Tu_p^2 + \frac{1}{4}C(1-C) \quad (7)$$

These analytical expressions (Eqs. (6) and (7)) were derived to estimate the water-phase turbulence intensity from total pressure fluctuations in both clear-water and aerated flows. Eq. (6) characterises the turbulent fluctuations in the water phase of a high-velocity air-water flow, which simplifies into Eq. (5) for a clear-water flow. Both Equations may be used with reasonable accuracy, except when Tu exceeds O(1) (Appendix I).

2.4. Experimental flow conditions

Total pressure and two-phase flow measurements were conducted for a range of discharges with a focus on the skimming flow regime ($d_c/h\geq0.9$). Both clear-water and two-phase measurements were undertaken at each step edge for $0.9\leq d_c/h\leq1.7$, corresponding to Reynolds numbers between 3.3×10^5 and 8.7×10^5. The experimental flow conditions are summarised in Table 1.

3. Flow patterns and developing flow region

3.1. Presentation

Visual observations indicated that the overflow consisted of a succession of free-falling nappes (i.e. nappe flow regime) for small discharges: i.e., $d_c/h<0.4$. For a range of intermediate flow rates, the flow motion appeared pseudo-chaotic with strong spray and splashing, and a combination of filled and partially-filled step cavities: i.e., a transition flow regime observed for $0.4\leq d_c/h<0.9$. For larger discharges ($d_c/h\ \geq0.9$), the flow skimmed as a coherent stream above the pseudo-invert formed by the step edges, as seen in Fig. 1. Beneath the pseudo-bottom, cavity recirculation was maintained through the transfer of momentum from the main stream to the recirculating motion. A significant amount of turbulent kinetic energy was dissipated to maintain the cavity circulation. For the remaining sections, the focus is on the skimming flow regime, typical of large prototype spillway operation (Fig. 1A).

At the upstream end of the chute, the skimming flow free-surface was smooth and no free-surface aeration took place (Fig. 1B). Once the outer edge of the developing boundary layer interacted with the free-surface, the flow was characterised by strong air bubble entrainment [9,12,50]. This location is known as the inception point of free-surface aeration, and divides the spillway flow into an upstream clear water developing flow region, and a downstream air-water fully-developed flow region. The flow in step cavities exhibited a pseudo-stable recirculation motion characterised by self-sustaining vortices. A close examination of the cavity vortical structures showed irregular ejection of fluid from the cavity into the mainstream flow next to the upper vertical step face, and replacement of cavity fluid next to the step edge, in manner similar to the observations of Djenidi et al. [21] and Chanson and Toombes [16].

3.2. Velocity, total pressure and turbulence intensity

In the developing flow region, the velocity data indicated a turbulent boundary layer with an ideal flow region above. In the ideal flow region, the flow was accelerated by gravity and the free-stream velocities followed closely theoretical estimates based upon the Bernoulli equation. Fig. 4 presents some typical distribution of time-averaged velocity and total pressure measured at step edges. Next to the pseudo-bottom, the velocity and total pressure distributions both showed a steep gradient because of effects of form drag. Above, the velocity and total head remained constant as predicted by the Bernoulli equation. The length of the developing flow region was seen to increase with increasing discharge. For $d_c/h>1.9$, no free-surface aeration was observed because the flow was partially-developed over the entire chute length.

All data showed large fluctuations in total pressure next to the pseudo-bottom formed by the step edges. This is illustrated in Fig. 5A, where $\overline{p_t^2}$ is the variance of the total pressure fluctuations. The total pressure fluctuations were the largest about $y/d_c\approx0.1$ and decreased towards the free-surface. The occurrence of this local maximum might be linked to vortices in the wake of the preceding step edge. Herein the largest dimensionless total pressure fluctuations were observed for the smallest discharge ($d_c/h=0.9$) corresponding to the shortest developing flow region (Fig. 5A). The turbulence intensity was derived from the total pressure fluctuation and time-averaged velocity data (Eq. (5)). Typical results are presented in Fig. 5B. In the developing

Table 1
Experimental flow conditions.

Ref.	Q (m^3/s)	d_c/h	Location	Comments	Instrumentation
Series 1	0.001–0.211	0.045–1.67	Step edges 1-12	Clear water and air-water flow regions	Visual observations.
Series 2	0.08F3–0.216	0.9–1.7	Step edges 3-9	Clear water flow region	Total pressure probe & Pitot tube.
Series 3	0.057–0.216	0.7–1.7	Step edges 5-12	Air-water flow region	Total pressure probe & Phase-detection probe.

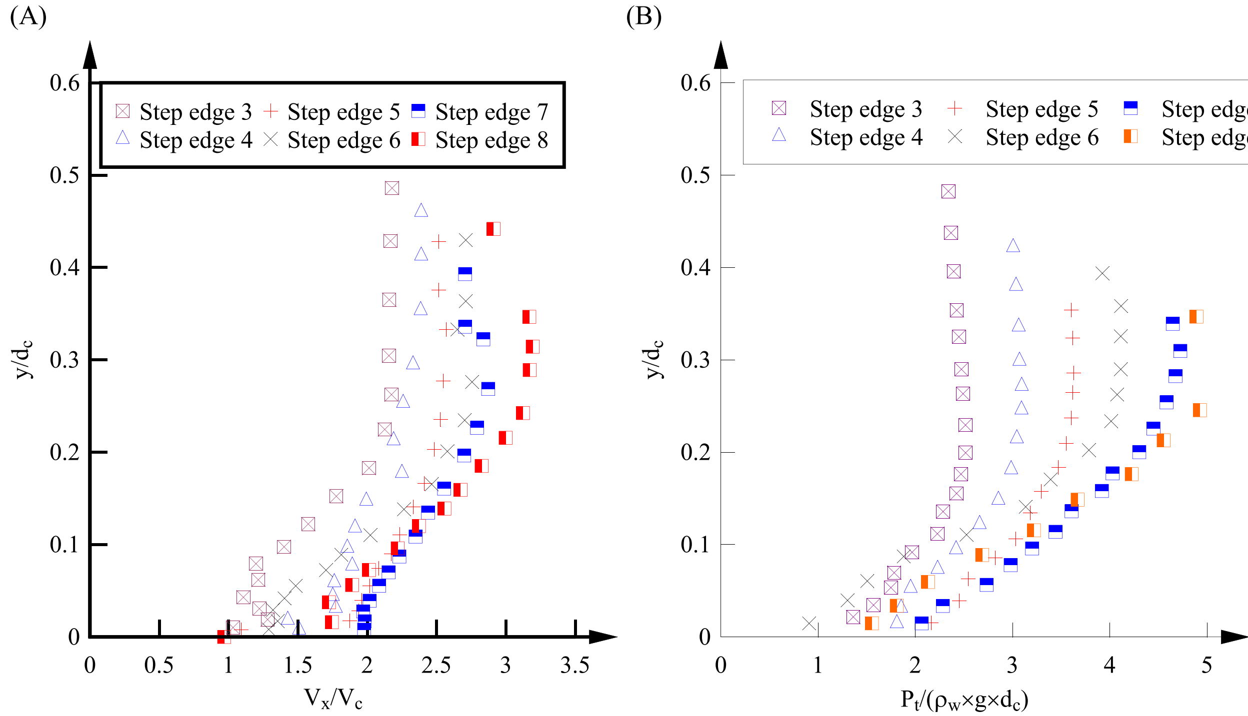

Fig. 4. Dimensionless distributions of time-averaged velocity and total pressure in the developing flow region of skimming flow - Flow conditions: $d_c/h = 1.7$, $Re = 8.7 \times 10^5$. (A) Streamwise velocity V_x, (B) Total pressure P_t.

boundary layer, the turbulence intensity Tu_p ranged between 0.05 and 0.45, with maxima next to the pseudo-bottom. In the ideal fluid flow region above, Tu_p was typically less than 0.05. The present results were quantitatively of the same order of magnitude as the results of Djenidi et al. [21] above d-type roughness using laser Doppler anemometry (LDA) and Amador et al. [1] above a stepped spillway model using particle image velocimetry (PIV).

In the present geometry, cavity recirculation vortices formed in the step cavities in a manner somehow similar to the classical d-type roughness [20,21,41]. The triangular cavity might however affect the main flow to a greater extent than a typical d-type

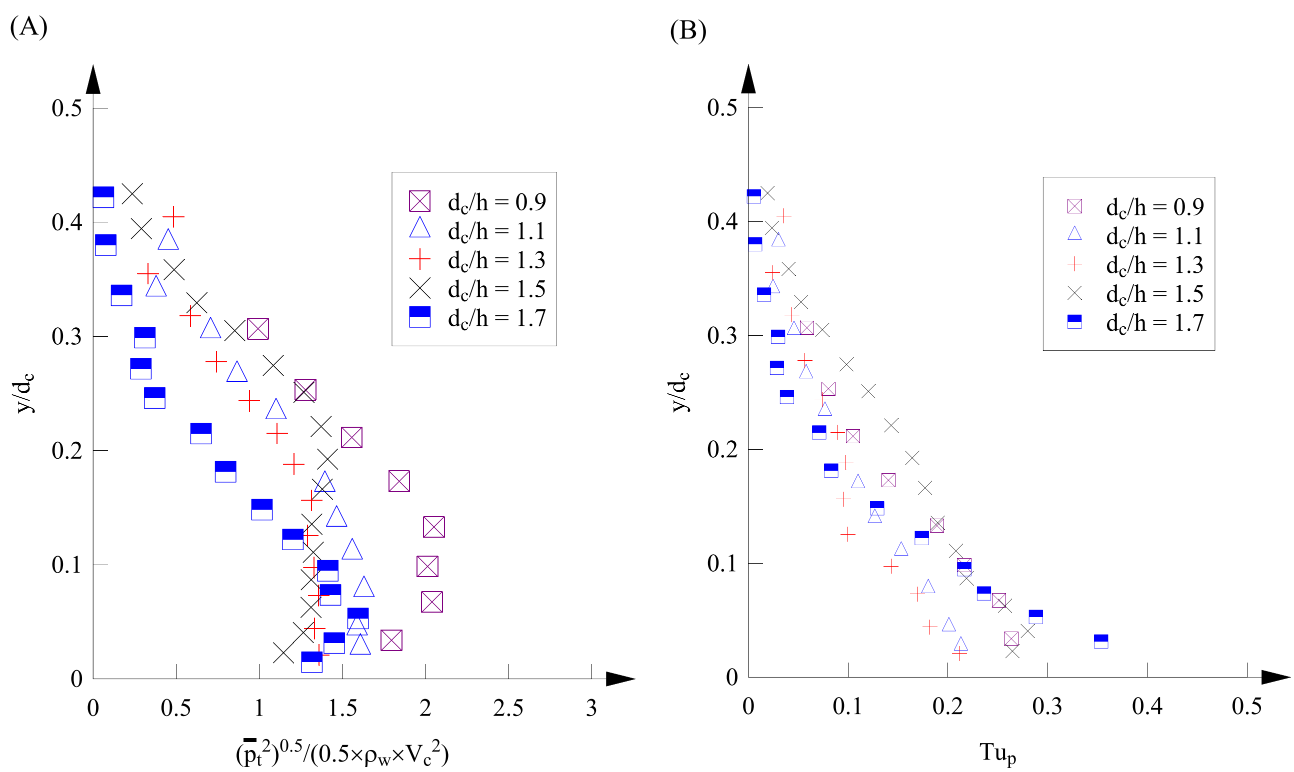

Fig. 5. Dimensionless distributions of total pressure fluctuations and turbulence intensity in the developing flow region of skimming flow at step edge 4. (A) Total pressure fluctuations $\sqrt{\overline{p_t^2}}$, (B) Turbulence intensity Tu_p.

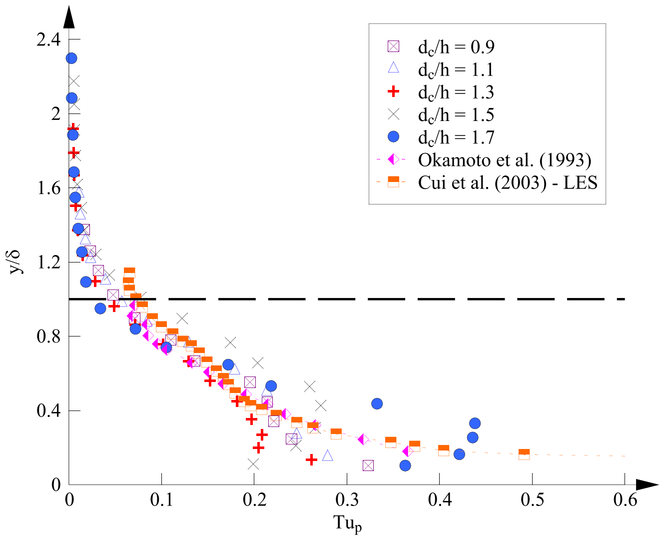

Fig. 6. Turbulence intensity distributions in the developing boundary layer (step edge 3) - Comparison with intermediate roughness data - Dashed line indicate the boundary layer thickness defined in terms of 99% of free-stream velocity.

ribbed roughness. At each step edge, the interactions between the overflow and the step edge induced separation and disturbances (eddies) convected by the mean flow. The mean flow properties in the overflow were thus altered through interactions with such eddies. When such vortical structures were produced at a faster rate than they were dissipated, the skimming flow properties were altered again before they are restored back to the undisturbed state. For these reasons, the overflow properties above each step cavity were likely to lack self-similarity and the present configuration might be more appropriately classified as an intermediate roughness, bearing characteristics similar to both d-type and k-type roughness [39,41]. Intermediate roughness flows were investigated experimentally by Okamoto et al. [40] and numerically by Cui et al. [18] using large eddy simulations (LES). Their results are compared to the present data in Fig. 6, and a good qualitative and quantitative agreement was achieved. Interestingly the turbulence intensity levels were non-negligible up to $y/\delta \approx 1.2$ to 1.4, with δ the boundary layer thickness, highlighting the fluctuating nature of the outer edge of the turbulent boundary layer [2,19,35,42,44].

3.3. Autocorrelation time and length scales

The autocorrelation time and length scales were characteristic scales of the largest eddies advected in the streamwise direction. In the developing flow region, they were estimated as:

$$T_{xx} = \int_0^{t_{Rxx=0}} R_{xx}(t)\ \mathrm{d}t \tag{8}$$

$$L_{xx} = V_x T_{xx} \tag{9}$$

where R is the normalised correlation coefficient of the total pressure, t is the time lag and it is implicitly assumed that the turbulent structures were convected at the same speed as the streamwise mean water velocity V_x. The auto-correlation time scale is an integral time scale that characterises the longest connections in the turbulent behaviour of the streamwise total pressure fluctuations. The auto-correlation length scale is an advection length scale that is a measure of the longest connection (or correlation distance) between the total pressures at two points of the flow field [32].

Dimensionless autocorrelation time and length scale distributions are presented in Fig. 7, where k_s denotes the step cavity roughness height: $k_s = h\cos\theta$ (=0.071 m herein). At step edge 3, the largest time and length scales were found around the mid-boundary layer ($y/\delta \approx 0.5$), except for the largest discharge. The characteristic eddy sizes were about three times the cavity roughness height, close to the data of Okamoto et al. [39] who obtained $L_{xx}/k_s \approx 2$ for various types of k-type triangular ribs. In the developing region, the flow was accelerated by gravity and vortices were stretched by the streamwise velocity gradient ($\partial V_x/\partial x$), explaining possibly the slightly larger results than Okamoto et al. [39]. Outside the boundary layer, the auto-correlation time and length scales were small. At the next step edge (step edge 4), the data showed a somewhat different pattern (Fig. 7). The locations of maximum time and length scales shifted towards the outer edge of the boundary layer, and larger time and length scales were recorded across the water column up to the free-surface. This lack of similarity might be linked to the highly fluctuating nature of the boundary layer and highlighted the complexity of the step-wake interactions over a stepped invert.

4. Fully-developed air-water flow region

4.1. Presentation

Downstream of the inception point of free-surface aeration, the flow was fully-developed and strong self-aeration was observed. This is illustrated in Fig. 8, showing typical distributions of time-averaged void fraction and interfacial velocity measured with the phase-detection probe. Herein the interfacial velocity was calculated based upon a cross-correlation technique [17]. The void fraction distributions showed an S-shape typically observed on stepped spillways with flat steps [16,27] (Fig. 8A). The data presented some self-similarity. In the overflow above the pseudo-bottom formed by the step edges, the void fraction data followed closely a theoretical model proposed by Chanson and Toombes [16] (Fig. 8A, solid line). The interfacial velocity data were approximated by a power law:

$$\frac{V_{aw}}{V_{90}} = \left(\frac{y}{Y_{90}}\right)^{1/N} \quad \left(\text{at step edge},\ 0 < y < Y_{90}\right) \tag{10}$$

where Y_{90} is the characteristic distance normal to the pseudo-bottom where $C = 0.9$, and V_{90} is the interfacial velocity at $y = Y_{90}$. For $y > Y_{90}$, the interfacial velocity distributions were essentially uniform and described by:

$$\frac{V_{aw}}{V_{90}} = 1 \quad \left(\text{at step edge},\ y/Y_{90} \geq 1\right) \tag{11}$$

The above relationships were compared to present experimental data, showing a satisfactory agreement for N=10 for all step edges (Fig. 8B), despite some scatter next to the inception point. In the vicinity of the inception point, the flow was subjected to rapid flow bulking.

4.2. Total pressure and turbulence intensity

In the air-water flows, the total pressure signal showed a distinct bimodal distribution because of the effects of air bubbles (Fig. 3). Typical distributions of time-averaged total pressure are presented in Fig. 9, and compared with the void fraction distribution. The data showed a maximum total pressure slightly below $y = Y_{50}$, where Y_{50} is a characteristic depth for $C = 0.5$.

Neglecting the air density and the capillary effects of wetting and drying (i.e. during interfacial interactions with probe sensor),

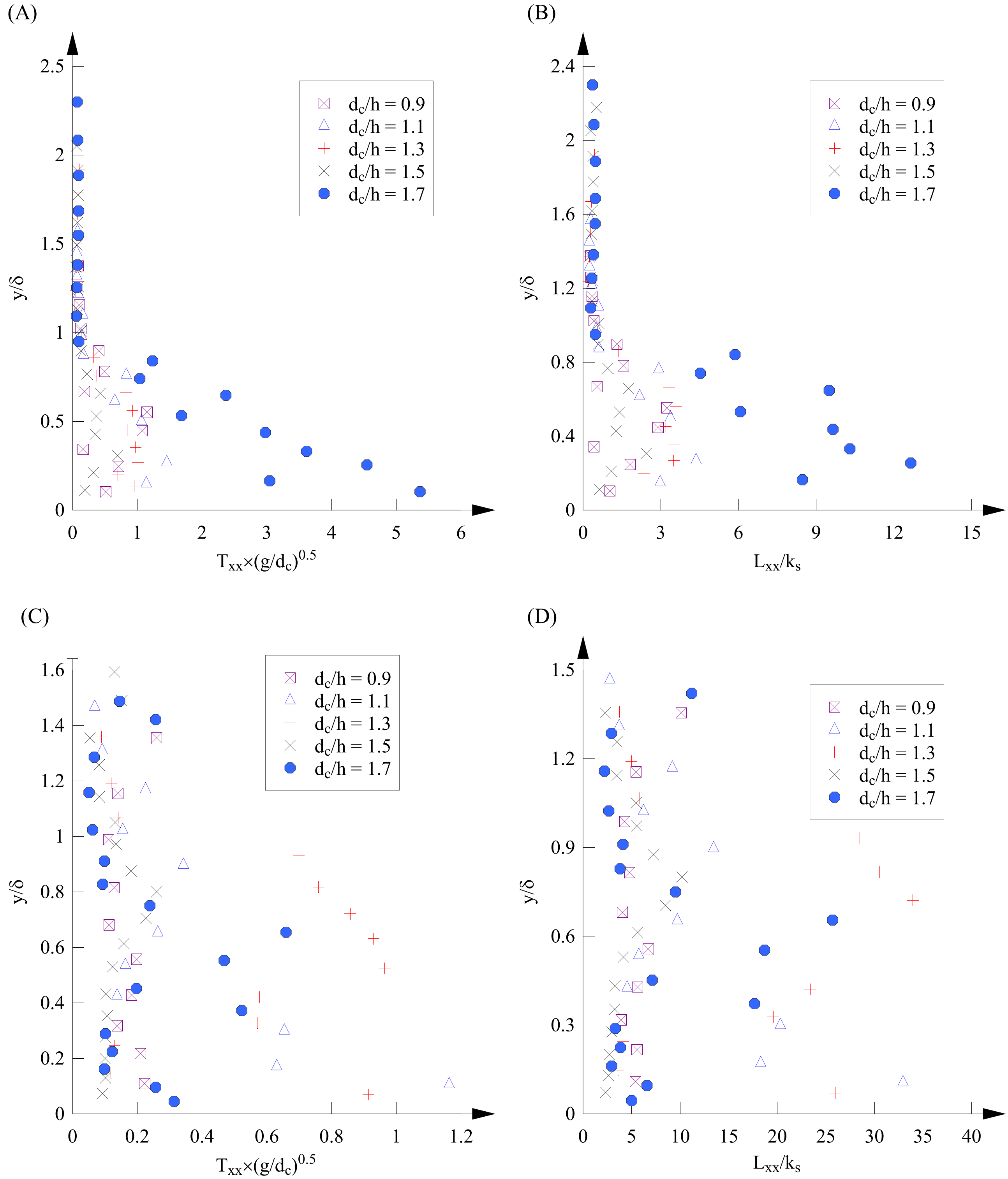

Fig. 7. Autocorrelation time and length scales in the developing flow region (step edges 3 and 4). (A) Streamwise integral time scale T_{xx}, step edge 3, (B) Advection length scale L_{xx}, step edge 3, (C) Streamwise integral time scale T_{xx}, step edge 4, (D) Advection length scale L_{xx}, step edge 4.

the mean total pressure may be expressed as:

$$P_t = P_k + P_s = \frac{1}{2}(1 - C)\rho_w\left(V_x^2 + \overline{v_x^2}\right) + P_s \tag{12}$$

where P_k is the mean kinetic pressure and P_s is the time-averaged static pressure. If the pressure gradient is hydrostatic, the time-averaged static pressure, P_s, may be deduced from the time-averaged void fraction distribution:

$$P_s = \rho_w g \cos\theta \int_y^{Y_{90}} (1 - C)\ dy \tag{13}$$

where y is the coordinate normal to the pseudo-bottom and θ is the angle between the pseudo-bottom and horizontal. Based upon Eq. (12), the kinetic pressure term (P_k) may be estimated from the phase-detection probe data (C and V_{aw}), if the time-averaged streamwise water velocity component V_x equals the interfacial

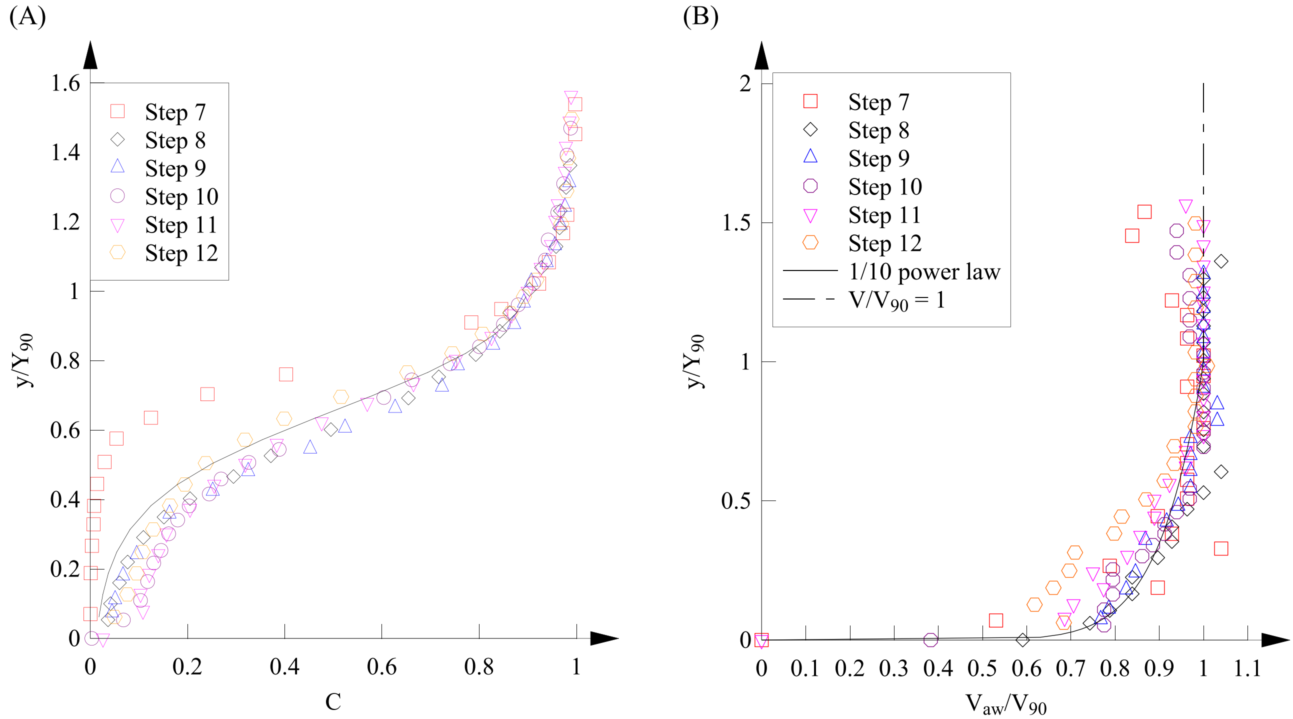

Fig. 8. Dimensionless distributions of time-averaged void fraction and interfacial velocity in the air-water fully-developed flow region for $d_c/h = 1.3$, $Re = 5.8 \times 10^5$. (A) Void fraction distributions, (B) Interfacial velocity distributions.

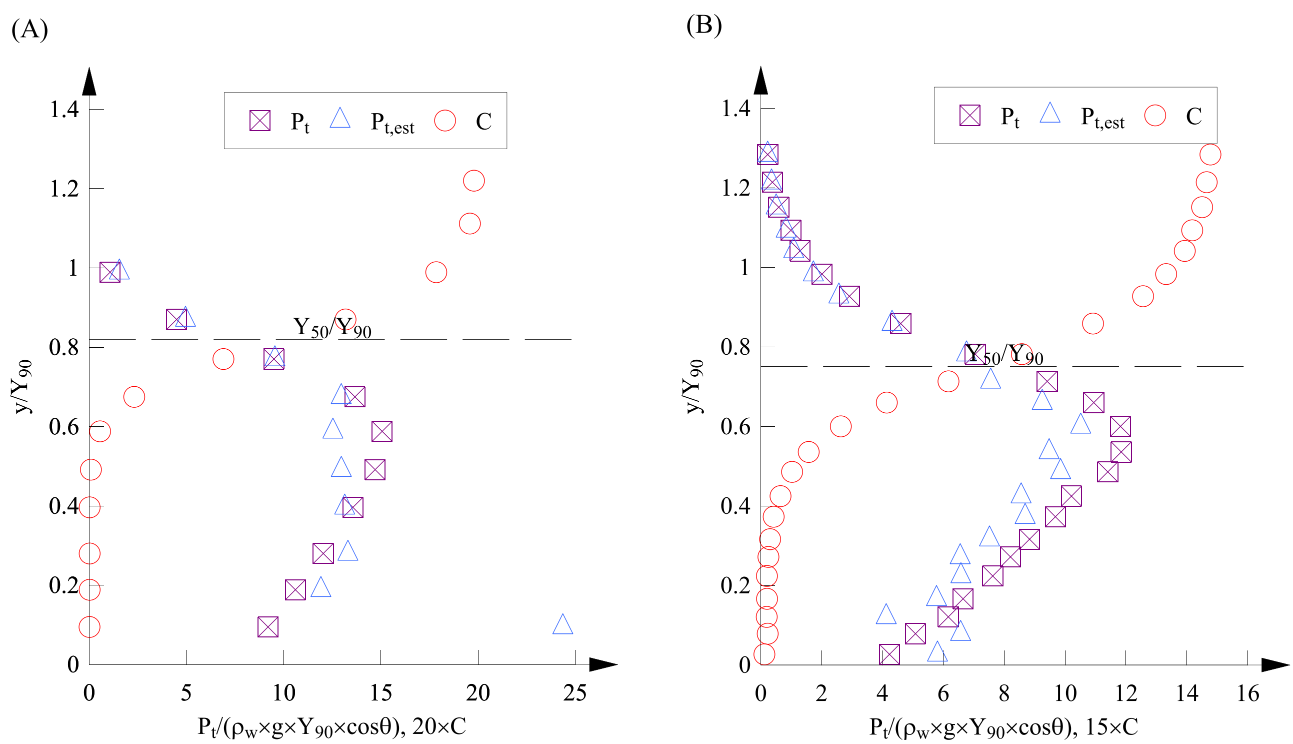

Fig. 9. Dimensionless distributions of total pressure and void fraction in the air-water fully-developed flow region of skimming flows - Comparison between total pressure data P_t and estimated total pressure $P_{t,est}$ based upon phase detection probe data - Dashed line indicates elevation Y_{50} where $C = 0.5$. (A) $d_c/h = 0.9$, $Re = 3.4 \times 10^5$, step edge 5, (B) $d_c/h = 1.7$, $Re = 8.7 \times 10^5$, step edge 12.

velocity V_{aw}, and the turbulence intensity is small ($\overline{v_x^2}/V_x^2 << 1$). Combining with the assumption of hydrostatic pressure distribution (Eq. (13)), an estimate of the mean total pressure may be derived from the phase-detection probe data, denoted $P_{t,\ est}$. Fig. 9 presents typical comparisons between the total pressure sensor data P_t and the estimate of mean total pressure $P_{t,\ est}$ based upon the phase-detection probe data. The present data set showed a good agreement between the measured and estimated total pressures (Fig. 9). The finding implied that a hydrostatic pressure distribution, taking into account the air entrainment (Eq. (13)), may be assumed in fully-developed air-water skimming flows. The close agreement between P_t and $P_{t,\ est}$ further implied that the

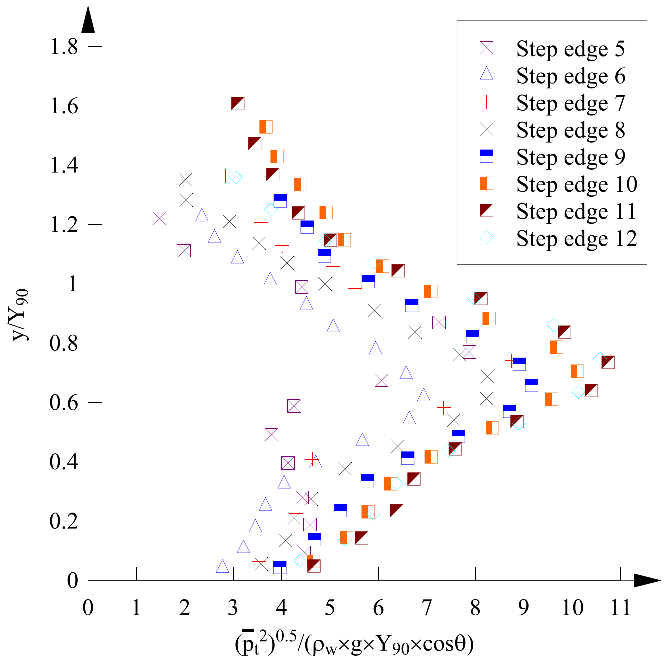

Fig. 10. Dimensionless distributions of total pressure fluctuations in the air-water fully-developed flow region of skimming flow - Flow conditions: $d_c/h=0.9$, $Re=3.4\times10^5$.

water phase turbulence intensity was small in aerated skimming flows ($Tu_p < 0.4$–0.5) (see discussion below).

Typical distributions of the root-mean-square (rms) of dimensionless total pressure fluctuations $\sqrt{\overline{p_t^2}}$ are presented in Fig. 10. The distributions presented a characteristic shape with a maximum about $y/Y_{90} \approx 0.7$. Next to the free-surface, moderate total pressure fluctuations were recorded (top most data points) but these data might be biased by capillary and interfacial effects during the droplet impacts onto the sensor.

The water phase turbulence intensity Tu_p may be derived from the total pressure signal and two-phase flow properties (Eq. (6)) (see Appendix I). Tu_p characterises the streamwise velocity fluctuations of the water phase. Typical data are presented in Fig. 11, where they are compared with interfacial turbulence intensity, calculated based upon cross-correlation of dual-tip phase detection probe signals [16]. Fig. 11A shows the water phase turbulence intensity Tu_p ranging between 0.1 and 0.5, irrespective of the discharge. Local maxima were found next to the pseudo-bottom ranging between 0.25–0.3, close to developing flow skimming flow data [1,38]. The turbulence intensity of the water phase presented a minimum value about 0.1–0.15 next to $y/Y_{90} \approx 0.5$ to 0.7. These minimum values were higher than those recorded at the outer edge of the developing boundary layer (5%, Section 3). For $y/Y_{90} > 0.5$–0.7, Tu_p increased with increasing distance from the pseudo-bottom. The relatively large values of Tu_p next to the free-surface might be partially attributed to the breaking surface with substantial water spray. The data trends are highlighted with black solid lines in Fig. 11. Typical interfacial turbulence intensities Tu deduced from a dual-tip phase-detection probe are presented in Fig. 11B. The interfacial turbulence intensities were systematically larger, ranging between 0.4 and 3.0. The data trends are also markedly different, as illustrated by the trend lines (thick solid lines) in Fig. 11. A systematic comparison between the two sets of data showed opposite trends, as seen in Fig. 11.

The present data trends (Fig. 11) might suggest that the velocity fluctuations of the water phase were damped by the presence of a large number of air bubbles in the mid-water column, because of surface tension and compressible nature of air. The direct contrast with the large interfacial turbulence intensities in that region might hint that the water particles and air-water interfaces fluctuated at different scales despite zero slip on average ($V_x \approx V_{aw}$). Considering the transport of a fluid particle under an instantaneous streamwise pressure gradient $-\partial\tilde{P}_s/\partial x$, assuming that the fluid behaves like an incompressible fluid and neglecting all other surface and body forces, the streamwise acceleration equals $-1/\rho \times \partial\tilde{P}_s/\partial x$, where ρ is the density of the fluid. Since the density

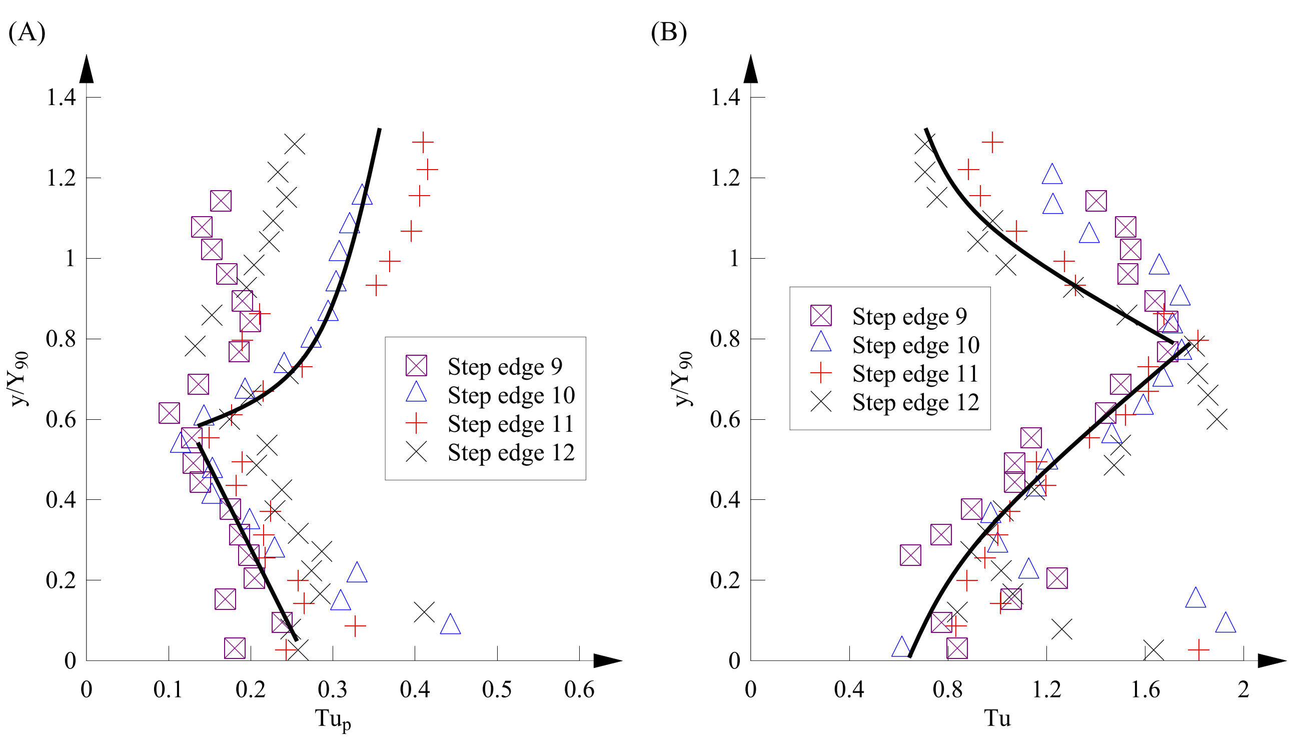

Fig. 11. Dimensionless distributions of turbulence intensity in the air-water fully-developed flow region of skimming flow: comparison between water phase turbulence intensity Tu_p and interfacial turbulence intensity Tu - Flow conditions: $d_c/h=1.7$, $Re=8.7\times10^5$. (A) Total pressure sensor data Tu_p, (B) Phase-detection probe data Tu.

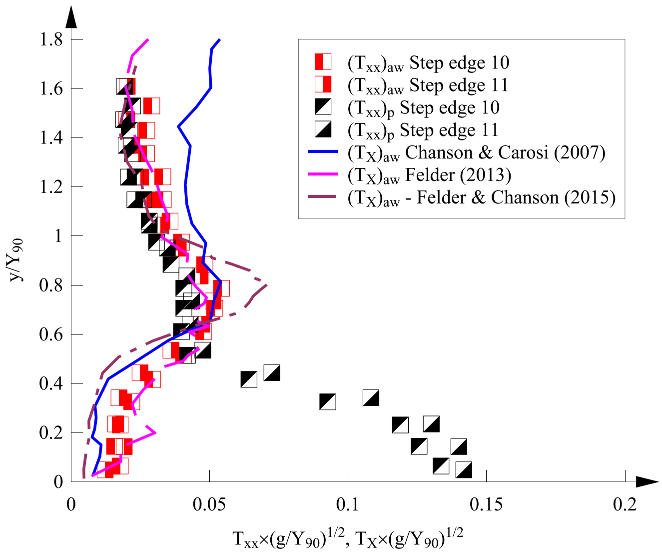

Fig. 12. Auto-correlation time scale distributions in the air-water fully-developed flow region of skimming flow - Comparison between phase-detection probe data and total pressure data (Present study, step edge 10), and integral turbulent time scale in air-water flows [15,26]

Reference	θ (°)	h (m)	d_c/h
Present study	45	0.10	0.9
Chanson and Carosi (2007)	21.8	0.10	1.33
Felder (2013)	8.9	0.05	3.0
Felder and Chanson (2015)	26.6	0.10	1.28

of water is approximately 800 times larger than that of air, the acceleration of an air particle is also 800 times larger. If the pressure gradient is uniform for a characteristic duration τ_c, an air particle moves 800 times the distance of a water particle of the same size during that time, if both particles start from rest. In reality, a number of processes including capillary forces and compressibility may contribute to a reduction in the difference between air and water velocity fluctuation scales. This simplistic discussion however underlines key distinctions between turbulent fluctuations of air and water phases.

4.3. Autocorrelation time and length scales

In the air-water flow region, the auto-correlation time and length scales were calculated based upon the instantaneous total pressure signal (subscript p) and the instantaneous void fraction (subscript aw). Typical results are shown in Fig. 12, where present data are compared with integral turbulent time scale data measured during previous relevant studies. Note that the physical interpretation of the time scales differs depending upon the data source. $(T_{xx})_{aw}$ characterised the time scale of the longitudinal interfacial structures advecting the air-water interfaces in the flow direction [15]. Present data showed a bell shape, with maximum values at $y/Y_{90} \approx 0.6$–0.8 (Fig. 12). All data tended to follow a self-similar distribution. In contrast, $(T_{xx})_p$ represented a characteristic time scale of the energy-containing eddies advected in the flow direction. The distributions of $(T_{xx})_p$ presented maxima next to the pseudo-bottom, and decreased monotonically up to $y/Y_{90} \approx 0.5$ (corresponding to $C=0.3$–0.4). At that location, the data trend showed a distinct change in slope, implying some physical change in the air-water flow structure. This location might approximately correspond to the upper bound of the shear layer created by the preceding step edge, below which the wake-step interactions might be significant.

The present data were compared to the turbulent integral time scale data of Chanson and Carosi [15], Felder [25] and Felder and Chanson [26] obtained in skimming flows on flat to moderate slopes (θ=8.9° to 26.6°). The results were quantitatively consistent with present findings, suggesting that the chute slope and discharge might have little influence of the interfacial structures. Such a strong self-similarity could be useful for extrapolation onto prototype structures, given Reynolds numbers sufficiently high to reproduce large-scale turbulent structures.

The distributions of auto-correlation length scales showed some self-similarity, with a trend close to those of the auto-correlation time scales. The data showed that the largest bubbly flow structures and energy-containing structures were respectively present in the mid-flow region and next to the pseudo-bottom. All data followed a self-similar distribution far downstream of the inception point. The length scales satisfied typically $L_{xx}/Y_{90} \approx 0.1$–$0.6$, with $(L_{xx})_p \approx (L_{xx})_{aw}$ for $y/Y_{90} > 0.6$. (data not shown).

5. Conclusion

The total pressure distributions were measured in the clear-water developing flow region and air-water fully-developed flow region above a steep stepped chute. These measurements were complemented by clear-water velocity measurements with a Pitot tube and air-water measurements with a dual-tip phase-detection probe. Analytical expressions were derived to estimate the water-phase turbulence intensity from total pressure fluctuations in both clear-water and aerated flows. The results were tested for five relatively large discharges corresponding to a skimming flow regime, and demonstrated the suitability of miniature total pressure probe in both clear-water and air-water flows.

Upstream of the inception point of free-surface aeration, the clear-water developing flow was characterised by a developing turbulent boundary layer and an ideal-flow region above. The potential flow velocity was well predicted by the Bernoulli equation. The boundary layer exhibited large total pressure fluctuations and turbulence intensities. The distributions of turbulence intensity were close to intermediate roughness flow data sets (i.e. intermediate between d-type and k-type).

The two-phase flow measurements provided time-averaged void fraction and interfacial velocity distributions, illustrating the interfacial air–water exchange next to the free surface. The total pressure measurements were validated in the highly-aerated turbulent shear region, since the total pressure predictions based upon the void fraction and velocity data agreed well with experimental results recorded by the total pressure probe. The static pressure exhibited a hydrostatic distribution, taking into account the void fraction distribution, in the air-water fully-developed flow region. The distributions of total pressure fluctuations showed a distinctive shape with a maximum about $y/Y_{90} \approx 0.7$. The data presented a contrast between the interfacial turbulence intensities and water phase turbulence intensities. The turbulence intensity in the water phase was typically smaller than the interfacial turbulence intensity, suggesting that velocity fluctuations of the water phase were damped by the presence of a large number of air bubbles because of surface tension and compressible nature of air. The auto-correlation time and length scale results were close to previous findings with different chute slopes and discharges, suggesting that these geometrical parameters might have little influence on the integral turbulent scales of the interfacial structures.

Acknowledgements

The authors acknowledge the technical assistance of Jason Van

Der Gevel and Stewart Matthews (The University of Queensland). They thank the reviewers for their helpful and constructive comments. The financial support through the Australian Research Council (Grant DP120100481) is acknowledged.

Appendix I. Total pressure signal analysis in air-water flows

The total pressure sensor measures the instantaneous total pressure aligned with the sensor, comprised of mean and fluctuating components:

$$\tilde{P}_t = \frac{1}{2}\tilde{\rho}\ \tilde{V}_x^2 + \tilde{P}_s \tag{I.1}$$

where $\tilde{P}_t$ is the instantaneous total pressure, $\tilde{\rho}$ is the instantaneous fluid density, $\tilde{V}_x$ is the instantaneous streamwise fluid velocity detected by the sensor, and $\tilde{P}_s$ is the instantaneous static pressure. In what follows capital and lower case letters are used to denote mean and fluctuating quantities; for example, $\tilde{P}_t = P_t + p_t$. While Ippen et al. [33] and Arndt and Ippen [3] proposed derivations for monophase flows (see below), the present appendix is focused on the signal analysis in high-velocity air-water flows.

In a two-phase flow, the total pressure output will show a distinct bimodal distribution because of the effects of air bubbles. This is seen in the probability density functions (PDF) of the total pressure probe signals, with a number of examples shown in Fig. 3. In Fig. 3, the first sensor signal PDF (C=0.008, purple line) shows a unimodal distribution because of the small number of air bubbles, while the other two PDFs exhibit large peaks next to zero, likely linked to air bubble impacts. When a submerged air bubble impacts the probe sensor, the effects include a kinetic pressure close to zero because air density is negligible compared to that of water, a static pressure increase inside the air bubble because of surface tension which becomes small compared to the kinetic pressure for bubble sizes greater than the millimetre, and capillary effects during wetting and drying processes that bias the signal.

Neglecting the air density and capillary effects, Eq. (I.1) may be decomposed into mean and fluctuating components and written separately for the individual phases. If the time-averaged void fraction C is interpreted as the probability of one signal sample being air, the classical time-average may be redefined as:

$$\overline{f(c,t)} = (1-C)\times\overline{f(c,t)|_{c_i=0}} + C\times\overline{f(c,t)|_{c_i=1}} \tag{I.2}$$

where f(c,t) is a function void fraction and time, and the overbar denotes a time-average operation. Applying Eq. (I.2) on Eq. (I.1), the mean total pressure becomes:

$$P_t = \frac{1}{2}(1-C)\ \rho_w\left(V_x^2 + \overline{v_x^2}\right) + P_s \tag{I.3}$$

where ρ_w is the water density. Similarly the total pressure fluctuation may be derived as:

$$\begin{aligned}\overline{p_t^2} = (1-C)\Bigg(&\frac{1}{4}\rho_w^2C^2V_x^4 + \rho_w^2V_x^2\overline{v_x^2} + \frac{1}{4}\rho_w^2\ \overline{v_x^4} + \frac{1}{4}(1-C)^2\rho_w^2\ \overline{v_x^2}^2\\ &+ \overline{p_s^2} + \frac{1}{2}\rho_w^2C\ V_x^2\overline{v_x^2} - \frac{1}{2}C(1-C)\\ &\rho_w^2V_x^2\overline{v_x^2} + \rho_w^2V_x\overline{v_x^3} + 2\ \rho_wV_x\overline{v_xp_s} - \frac{1}{2}(1-C)\ \rho_w^2\ \overline{v_x^2}^2 + \rho_w\overline{v_x^2p_s}\Bigg)\\ &+ C\left(\frac{1}{4}(1-C)^2\rho_w^2\left(V_x^4 + 2\ V_x^2\overline{v_x^2} + \overline{v_x^2}^2\right) + \overline{p_s^2}\right)\end{aligned} \tag{I.4}$$

If the static pressure and streamwise velocity fluctuations, respectively p_s and v_x, are each normally distributed with zero mean, and denoting $r_{pu} = \overline{p_sv_x}/\left(\sqrt{\overline{v_x^2}}\ \sqrt{\overline{p_s^2}}\right)$ their normalised correlation coefficient, Eq. (I.4) may be simplified into [29]:

$$\begin{aligned}\overline{p_t^2} = &\Bigg(\frac{1}{4}\rho_w^2C^2V_x^4 + \rho_w^2\left(1 + \frac{1}{2}C^2\right)V_x^2\ \overline{v_x^2} + \rho_w^2\left(\frac{1}{2} + \frac{C^2}{4}\right)\overline{v_x^2}^2\\ &+ 2\ r_{pu}\rho_wV_x\sqrt{\overline{v_x^2}}\sqrt{\overline{p_s^2}}\Bigg)\ (1-C)\\ &+ \left(\frac{1}{4}(1-C)^2\rho_w^2\left(V_x^4 + 2\ V_x^2\overline{v_x^2} + \overline{v_x^2}^2\right)\right)\ C + \overline{p_s^2}\end{aligned} \tag{I.5}$$

For an irrotational flow field, Bradshaw [6] demonstrated the relationship between pressure and velocity fluctuations, showing that the static pressure fluctuations include contributions from both irrotational velocity fluctuations and flow convection and yielding a negative correlation coefficient r_{pu}. In the initial region of a plane turbulent wind jet, Guo and Wood [28] observed $r_{pu} \approx -0.25$ in the turbulent zone away from the jet core. Given that the presence of air bubbles might provide some 'cushioning' damping, it is proposed that $r_{pu} = -0.1$, which is yet to be experimentally justified. (As part of preliminary tests, no major difference ($<5\%$) was observed for $-0.5 < r_{pu} < -0.05$ in terms of turbulence intensity.) In a field of homogeneous and isotropic turbulence with very large Reynolds numbers, the mean-square pressure fluctuation can be expressed in terms of the mean-square velocity fluctuation [4]:

$$\overline{p_s^2} = 0.34\rho_w^2\ \overline{v_x^2}^2 \tag{I.6}$$

Considering Eq. (I.6) as a crude approximation, and assuming $r_{pu} = -0.1$, the relationship between total pressure fluctuation and turbulence intensity $Tu_p = \sqrt{\overline{v_x^2}}/V_x$ become in air-water flows:

$$\begin{aligned}\frac{\overline{p_t}^2}{\rho_w^2V_x^4} = &\left((1-C)\left(\frac{1}{2} + \frac{C}{4}\right) + 0.34(1-C)^2\right)Tu_p^4\\ &- 0.116(1-C)^2Tu_p^3 + (1-C)\left(1 + \frac{1}{2}C\right)Tu_p^2\\ &+ \frac{1}{4}C(1-C)\end{aligned} \tag{I.7}$$

If the higher order terms (i.e. Tu_p^3, Tu_p^4) are neglected (e.g. $Tu_p \le 0.4$-0.5), the following approximate form holds:

$$Tu_p = \sqrt{\frac{\frac{\overline{p_t^2}}{\rho_w^2V_x^4} - \frac{(1-C)C}{4}}{(1-C)\left(1 + \frac{C}{2}\right)}} \tag{I.8}$$

Eq. (I.7) must be used if Tu_p approaches or exceeds O(1). For clear water flow (C=0), Eq. (I.8) becomes:

$$\frac{\overline{p_t^2}}{\rho_w^2V_x^4} = Tu_p^2 \tag{I.9}$$

Eq. (I.9) assumed implicitly that the static pressure fluctuations are negligible, as these are a higher order term in Eq. (I-7).

Following Ippen et al. [33], Arndt and Ippen [3] used a similar approach and obtained an expression in monophase flows:

$$\frac{\overline{p_t^2}}{\rho_wV_x^4} < Tu_p^2 + Tu_p^3 + \frac{5}{4}Tu_p^4 \tag{I.10}$$

Eq. (I.10) is identical to (I.9) if the higher order terms are neglected and the operator '<' is replaced by '='. The main difference between their work and the present lies in the treatment of the calculations of expected values of the products of the fluctuating terms. Arndt and Ippen [3] assumed:

$$\overline{p_s v_x} < \frac{\rho_w}{2}\overline{v_x^2}^{3/2} \tag{I.11a}$$

$$\overline{p_s v_x^2} < \frac{\rho_w}{2}\overline{v_x^2}^{2} \tag{I.11b}$$

$$\overline{p_s^2} < \frac{\rho_w^2}{4}\overline{v_x^2}^{2} \tag{I.11c}$$

While Eqs. (I.11a) and (I.11b) are correct, Eq. (I.11c) contradicts Batchelor's [4] hypothesis for isotropic turbulence with Re $\rightarrow +\infty$ (Eq. (I.6)).

In summary, analytical expressions were derived to estimate the water-phase turbulence intensity from total pressure fluctuations in both clear water and aerated flows. Eq. (I.8) characterises the turbulent fluctuations in the water phase of a high-velocity air-water flow, which simplifies into Eq. (I.9) for a clear water flow. Both Equations may be used with reasonable accuracy, except when Tu exceeds O(1).

References

[1] A. Amador, M. Sanchez-Juny, J. Dolz, Characterization of the nonaerated flow region in a stepped spillway by PIV, J. Fluids Eng. ASME 128 (6) (2006) 1266–1273.

[2] R.A. Antonia, Conditionally sampled measurements near outer edge of a turbulent boundary layer, J. Fluid Mech. 56 (1) (1972) 1–18.

[3] R.E.A. Arndt, A.T. Ippen, Turbulence measurements in liquids using an improved total pressure probe, J. Hydraul. Res. 8 (2) (1970) 131–158, http://dx.doi.org/10.1080/00221687009500300.

[4] G.K. Batchelor, Pressure fluctuations in isotropic turbulence, Math. Proc. Camb. Philos. Soc. 47 (2) (1951) 359–374, http://dx.doi.org/10.1017/s0305004100026712.

[5] F.A. Bombardelli, Computational Multi-Phase Fluid Dynamics to Address Flows past Hydraulic Structures. Proc. 4th IAHR International Symposium on Hydraulic Structures, APRH - Associação Portuguesa dos Recursos Hídricos (Portuguese Water Resources Association), J. Matos, S. Pagliara & I. Meireles Eds., 9-11 February 2012, Porto, Portugal, Paper 2, 19 pages (CD-ROM).

[6] P. Bradshaw, Turbulence, Topics in Applied Physics, Springer-Verlag, Berlin, Germany 1976, p. 335.

[7] P. Cain, I.R. Wood, Measurements of self-aerated flow on a spillway, J. Hydraul. Div. 107 (1981) 1425–1444.

[8] P. Cain, I.R. Wood, Instrumentation for aerated flow on spillways, J. Hydraul. Div. ASCE 107 (HY11) (1981) 1407–1424.

[9] M.R. Chamani, N. Rajaratnam, Characteristics of skimming flow over stepped spillways, J. Hydraul. Eng. ASCE 125 (4) (1999) 361–368.

[10] K.A. Chang, H.J. Lim, C.B. Su, Fiber optic reflectometer for velocity and fraction ratio measurements in multiphase flows, Rev. Sci. Instrum. 74 (2003) 3559–3565, Discussion: 2004, 75:284-286.

[11] H. Chanson, Comparison of energy dissipation between nappe and skimming flow regimes on stepped chutes, J. Hydraul. Res. IAHR 32 (2) (1994) 213–218.

[12] H. Chanson, Hydraulics of skimming flows over stepped channels and spillways, J. Hydraul. Res. IAHR 32 (3) (1994) 445–460.

[13] H. Chanson, Air-water flow measurements with intrusive phase-detection probes. Can we improve their interpretation ? J. Hydraul. Eng. 128 (2002) 252–255.

[14] H. Chanson, Turbulent air-water flows in hydraulic structures: dynamic similarity and scale effects, Environ. Fluid Mech. 9 (2) (2009) 125–142, http://dx.doi.org/10.1007/s10652-008-9078-3.

[15] H. Chanson, G. Carosi, Turbulent time and length scale measurements in high-velocity open channel flows, Exp. Fluids 42 (3) (2007) 385–401, http://dx.doi.org/10.1007/s00348-006-0246-2.

[16] H. Chanson, L. Toombes, Air-water flows down stepped chutes: turbulence and flow structure observations, Int. J. Multiph. Flow. 27 (2002) 1737–1761.

[17] C. Crowe, M. Sommerfield, Y. Tsuji, Multiphase Flows with Droplets and Particles, CRC Press, Boca Raton, USA 1998, p. 471.

[18] J. Cui, V.C. Patel, C. Lin, Large-eddy simulation of turbulent flow in a channel with rib roughness, Int. J. Heat. Fluid Flow. 24 (3) (2003) 372–388, http://dx.doi.org/10.1016/s0142-727x(03)00002-x.

[19] H.W. Daily, D.R.F. Harleman, Fluid dynamics, Reading, Mass, Addison-Wesley Publishing, USA 1966, p. 454.

[20] L. Djenidi, F. Anselmet, R.A. Antonia, LDA measurements in a turbulent boundary layer over a d-type rough wall, Exp. Fluids 16 (1994) 323–329.

[21] L. Djenidi, R. Elavarasan, R.A. Antonia, The turbulent boundary layer over transverse square cavities, Jl Fluid Mech. 395 (1999) 271–294.

[22] D.A. Drew, S.L. Passman, Theory of multicomponent fluids, in: J.E. Marsden, L. Sirovich (Eds.), Applied Mathematical Sciences, 135, Springer, New York, USA, 1999, p. 308.

[23] R. Ehrenberger, Wasserbewegung in steilen Rinnen (Susstennen) mit besonderer Berucksichtigung der Selbstbelüftung. ('Flow of Water in Steep Chutes with Special Reference to Self-aeration.') Zeitschrift des Österreichischer Ingenieur und Architektverein, (15/16 and 17/18 (in German) (translated by Wilsey, E.F., U.S. Bureau of Reclamation), 1926.

[24] D.A. Ervine, H.T. Falvey, Behaviour of turbulent water jets in the atmosphere and in plunge pools, Proc. Inst. Civil. Eng. Lond. 2 83 (1987) 295–314.

[25] S. Felder, Air-Water Flow Properties on Stepped Spillways for Embankment Dams: Aeration, Energy Dissipation and Turbulence on Uniform, Non-Uniform and Pooled Stepped Chutes. pH.D. thesis, School of Civil Engineering, The University of Queensland, Brisbane, Australia, 2013.

[26] S. Felder, H. Chanson, Phase-detection probe measurements in high-velocity free-surface flows including a discussion of key sampling parameters, Exp. Therm. Fluid Sci. 61 (2015) 66–78, http://dx.doi.org/10.1016/j.expthermflusci.2014.10.009.

[27] C.A. Gonzalez, H. Chanson, Interactions between cavity flow and main stream skimming flows: an experimental study, Can. J. Civ. Eng. 31 (1) (2004) 33–44.

[28] Y. Guo, D.H. Wood, Instantaneous velocity and pressure measurements in turbulent mixing layers, Exp. Therm. Fluid Sci. 24 (3–4) (2001) 139–150, http://dx.doi.org/10.1016/s0894-1777(01)00046-2.

[29] J.B.S. Haldane, Moments of the distributions of powers and products of normal variates, Biometrika 32 (3/4) (1942) 226, http://dx.doi.org/10.1093/biomet/32.3-4.226.

[30] T.J. Hanratty, T. Theofanous, J.M. Delhaye, J. Eaton, J. McLaughlin, A. Prosperetti, S. Sundaresan, G. Tryggvason, Workshop findings, Int. J. Multiph. Flow. 29 (2003) 1047–1059, http://dx.doi.org/10.1016/S0301-9322(03)00068-5.

[31] F.M. Henderson, Open Channel Flow, MacMillan Company, New York, USA, 1966.

[32] J.O. Hinze, Turbulence, 2nd edition, McGraw-Hill Publ, New York, USA, 1975.

[33] A.T. Ippen, R.S. Tankin, F. Raichlen, Turbulence Measurements in Free Surface Flow with an Impact Tube-Pressure transducer Combination. Technical Report (20, Hydrodynamics Laboratory, MIT, USA,1955, p. 96.

[34] R.J. Keller, A.K. Rastogi, Prediction of flow development on spillways, J. Hydraul. Div. ASCE 101 (HY9) (1975) 1171–1184.

[35] P.S. Klebanoff, Characteristics of Turbulence in a Boundary Layer with Zero Pressure Gradient. NACA Report 1247, 1955, p. 20.

[36] I. Meireles, F. Renna, J. Matos, F.A. Bombardelli, Skimming, nonaerated flow on stepped spillways over roller compacted concrete dams, J. Hydraul. Eng. ASCE 138 (10) (2012) 870–877.

[37] P. Novak, A.I.B. Moffat, C. Nalluri, R. Narayanan, Hydraulic Structures, 2nd edition, E & FN Spon, London, UK 1996, p. 599.

[38] I. Ohtsu, Y. Yasuda, Characteristics of flow conditions on stepped channels, in: Proceedings of the 27th IAHR Biennial Congress, San Francisco, USA, Theme D, 1997, pp. 583–588.

[39] S. Okamoto, S. Seo, S. Nakaso, S. Morishita, S. Namiki, Effect of sectional shape of rib on turbulent shear flow over rows of two-dimensional ribs on a ground plane, in: Proc. 11th Australasian Fluid Mechanics Conference, Hobart Australia, 1, 1992, pp. 539–542.

[40] S. Okamoto, S. Seo, K. Nakaso, I. Kawai, Turbulent shear flow and heat transfer over the repeated two-dimensional square ribs on ground plane, J. Fluids Eng. Trans. ASME 115 (4) (1993) 631–637, http://dx.doi.org/10.1115/1.2910191.

[41] A.E. Perry, W.H. Schofield, P.N. Joubert, Rough wall turbulent boundary layers, J. Fluid Mech. 37 (2) (1969) 383–413, http://dx.doi.org/10.1017/s0022112069000619.

[42] W.R.C. Phillips, J.T. Ratnanather, The outer region of a turbulent boundary layer, Phys. Fluids A-Fluid Dyn. 2 (3) (1990) 427–434.

[43] N.S.L. Rao, H.E. Kobus, Characteristics of Self-Aerated Free-Surface Flows. Water and Waste Water/Current Research and Practice, Eric Schmidt Verlag, Berlin, Germany, 1971.

[44] H. Schlichting, Boundary Layer Theory, 7th edition, McGraw-Hill, New York, USA, 1979.

[45] L. Toombes, Experimental Study of Air-Water Flow Properties on Low-Gradient Stepped Cascades, pH.D. thesis, Dept of Civil Engineering, The University of Queensland,, Brisbane, Australia, 2002.

[46] USBR, Design of Small Dams. Bureau of Reclamation, 1st edition, US Department of the Interior, Denver, CO, USA, 1965, 3rd printing.

[47] H. Wang, F. Murzyn, H. Chanson, Total Pressure Fluctuations And Two-phase Flow Turbulence In Hydraulic Jumps, Exp. Fluids 55 (11) (2014) 16, http://dx.doi.org/10.1007/s00348-014-1847-9.

[48] I.R. Wood, Air Entrainment in Free-Surface Flows. IAHR Hydraulic Structures Design Manual (4, Hydraulic Design Considerations, Balkema Publ, Rotterdam, The Netherlands 1991, p. 149.

[49] I.R. Wood, P. Ackers, J. Loveless, General method for critical point on spillways, J. Hydraul. Eng. ASCE 109 (2) (1983) 308–312.

[50] G. Zhang, H. Chanson, Hydraulics of the Developing Flow Region of Stepped Cascades: an Experimental Investigation. Hydraulic Model Report No. CH97/15, School of Civil Engineering, The University of Queensland, Brisbane, Australia, 2015, p. 76.